Nuclear Engineering and Technology 53 (2021) 1259–1265

Contents lists available at ScienceDirect

Nuclear Engineering and Technology

journal homepage: www.elsevier.com/locate/net

Original Article

Design and performance prediction of large-area hybrid gamma imaging system (LAHGIS) for localization of low-level radioactive material

Hyun Su Lee [a], Jae Hyeon Kim [a, b], Junyoung Lee [a], Chan Hyeong Kim [a, *]

[a] Department of Nuclear Engineering, Hanyang University, Seoul, 04763, South Korea
[b] Radiation Research Division, Korea Atomic Energy Research Institute, Jeongeup, 56121, South Korea

ARTICLE INFO

Article history:
Received 30 March 2020
Received in revised form
7 August 2020
Accepted 14 September 2020
Available online 22 September 2020

Keywords:
Coded aperture
Compton camera
Hybrid imaging
Monte Carlo simulation

ABSTRACT

In the present study, a large-area hybrid gamma imaging system was designed by adopting coded aperture imaging on the basis of a large-area Compton camera to achieve high imaging performance throughout a broad energy range (100–2000 keV). The system consisting of a tungsten coded aperture mask and monolithic NaI(Tl) scintillation detectors was designed through a series of Geant4 Monte Carlo radiation transport simulations, in consideration of both imaging sensitivity and imaging resolution. Then, the performance of the system was predicted by Geant4 Monte Carlo simulations for point sources under various conditions. Our simulation results show that the system provides very high imaging sensitivity (i.e., low values for minimum detectable activity, MDA), thus allowing for imaging of low-activity sources at distances impossible with coded aperture imaging or Compton imaging alone. In addition, the imaging resolution of the system was found to be high (i.e., around 6°) over the broad energy range of 59.5–1330 keV.

1. Introduction

Gamma-ray imaging techniques have been developed for different applications. Some applications such as industrial survey and environmental remediation can benefit from very high imaging sensitivity with moderately high imaging resolution over a broad energy range [1]. The large-area Compton camera (LACC) [2] was developed under such sensitivity and resolution demands by employing large-area scintillation detectors, in contrast to the majority of other Compton cameras using small detectors for hand-held portability [3–9]. The LACC has the advantage of 3-D imaging capability for near-field imaging, as well as very high imaging sensitivity owing to its large detectors [2]. However, like other Compton cameras, the LACC suffers from performance degradation at low energies, which is an inherent limitation of the imaging method utilizing Compton kinematics [10]. For example, the LACC shows only a few percent of imaging sensitivity for 140 keV (^{99m}Tc) compared to that of 662 keV (^{137}Cs), and such limitation makes it impractical to image low energy gamma ray sources such as ^{241}Am (59.5 keV) and ^{57}Co (122 keV) with the LACC.

Such energy dependency is commonly observed in most radiation imaging systems relying on mechanical or electronic collimation. Multi-modality imaging, also known as hybrid imaging, was proposed to solve the problem of energy dependency by combining mechanical and electronic collimation [10], and its efficacy has been proved by several studies [11,12].

In the present study, a large-area hybrid gamma imaging system (LAHGIS) is designed by adopting coded aperture imaging on the basis of the LACC to achieve not only high imaging performance (imaging resolution and sensitivity) throughout a broad energy range (100–2000 keV) but also mobility of system. A modified uniformly redundant array (MURA) [13] collimator is used for coded aperture imaging because it has been well established by researches in many fields [14,15] and the combination of MURA with Compton imaging also has been proved to be beneficial [11]. The LAHGIS is designed through a series of Geant4 Monte Carlo simulations in consideration of both imaging sensitivity and imaging resolution. Then, the performance of the designed system is predicted again by Geant4 Monte Carlo simulations for some point sources under different conditions of source activity, photon

* Corresponding author. 222 Wangsimni-ro, Seongdong-Gu, Seoul, 04763, South Korea.
E-mail address: chkim@hanyang.ac.kr (C.H. Kim).

https://doi.org/10.1016/j.net.2020.09.008

energy, and source position.

2. System design

The LAHGIS consists of two position-sensitive scintillation detectors and a coded aperture mask, as shown in Fig. 1. Each of the detectors, inheriting its design from the LACC [2], is composed of a 27×27 cm^2 monolithic NaI(Tl) scintillator crystal coupled with an array of 36 photo-multiplier tubes [16]. The thickness of the crystal is 2 cm and 3 cm for the frond and the back detector, respectively. Two detectors are placed as close as possible, which makes the distance between the detector faces to be 25 cm. The detectors offer an energy resolution of 7.9% for a 662-keV gamma-ray and a spatial resolution of 5 mm. The detailed design of the LACC detectors can be found elsewhere [16].

The collimator mask was designed based mostly on the knowledge of coded aperture imaging that has been established in the literature [17,18] and in consideration of the characteristics of the front detector of the LACC, which is close to the collimator mask. The mask was formed by arranging tungsten elements in a pattern of a 2×2 mosaic of 19×19 MURA. The size of the mask was chosen as 27×27 cm^2, which matches the front surface of the scintillator crystal of the front detector and also corresponds to the maximum size that enables the mask to rotate within the boundary of the detector casing for potential application of background suppression by the mask-antimask technique [19]. The separation distance between the mask and the front detector was set to 6 cm so that the coded aperture imaging can offer a field of view (FOV) of 130°, as wide as that of the LACC.

The thickness of the mask, on the other hand, was determined with further consideration of its impact on the performance of the imaging system. For example, a thicker mask may improve the image contrast of coded aperture imaging at higher energy, but it may also increase artifacts for off-axis source positions on the coded aperture imaging [17] and decrease Compton imaging sensitivity by blocking gamma rays. Hence, the thickness of the mask was selected based on a series of simulation studies, as described in section 4 below.

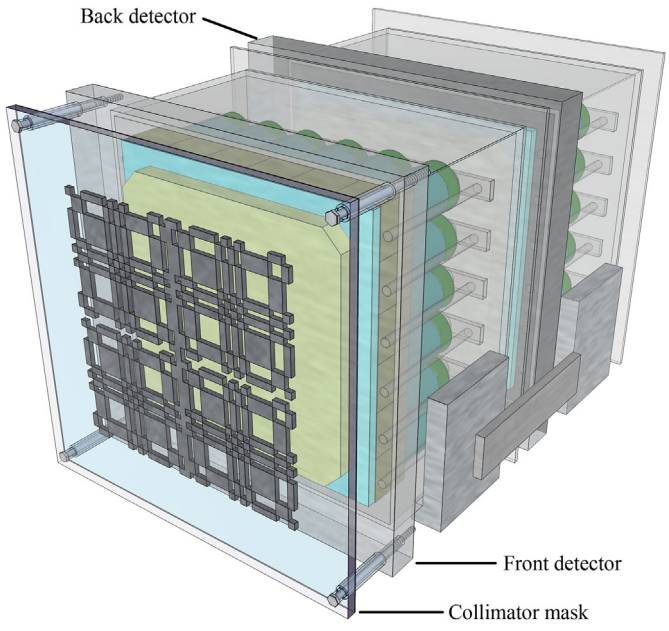

Fig. 1. Large-area hybrid gamma imaging system design consisting of two position-sensitive NaI(Tl) scintillation detectors and MURA coded aperture mask.

The Geant4 Monte Carlo simulation toolkit [20] (version 10.04) was used for both determination of mask thickness and performance prediction. The detectors and the mask, composing the LAHGIS, were modeled in Geant4. The thickness of the mask was set to be adjustable. A background radiation model [21] constructed based on the energy spectra measured with the detectors was employed. In Geant4 simulations, detection process was simplified; the interaction position (x, y) and deposited energy information of the photon interactions in the detectors was recorded event by event, rather than considering detailed behavior of scintillation and signal generation in the PMTs. Instead, to simulate the uncertainties that occur when estimating interaction position and energy from multiple PMT signals in the actual detectors, random error was generated according to the position and energy resolution of the detectors, and added to the recorded data. Then, the data were used to reconstruct emission images with an in-house MATLAB program.

3. Image reconstruction

In the present study, images were reconstructed using three imaging methods: coded aperture imaging, Compton imaging, and hybrid imaging, for each of which, the maximum-likelihood expectation-maximization (ML-EM) algorithm [22] was used, given by

$$\lambda_j^{n+1} = \lambda_j^n \frac{\sum_i c_{ij} Y_i / \sum_k c_{ik} \lambda_k^n}{S_j}$$

where λ_j^n is the image intensity of image pixel j at the nth iteration, Y_i is the count of detector pixel i, the system matrix, which indicates the probability that a photon emitted from image pixel j will be detected at detector pixel i, and S_j is the sensitivity image, defined as the detection probability of a photon from image pixel j.

For calculation of the S_j for Compton imaging, we adopted the method proposed by Muñoz et al. [23] that utilized Monte Carlo integration to calculate the sensitivity image of a Compton camera. It calculated the S_j by integrating the probabilities of events generated by sampling points from the image space and the detectors. The S_j and c_{ij} for the coded aperture imaging were also calculated in the same manner. In these calculations, a simplified geometry comprising the mask and the scintillator crystals was considered, and the probabilities of the sampled events were calculated according to the imaging principles as described below, whereas solid angle and attenuation from the mask and the crystal were considered in common among the three modes.

1) Coded Aperture Imaging
   Events wherein the photon was fully absorbed in the front detector were used. The c_{ij} was calculated for every image pixel and interaction position bin in the detector, considering the probability of photoelectric absorption after the photon reached the sampled point. The S_j was calculated by summing the c_{ij} values over the positions in the detector.
2) Compton Imaging
   The coincidence events, for which the photon had interaction in both detectors, were used. The c_{ij} was calculated only for measured events, i.e. list-mode ML-EM, instead of considering every possible event. The S_j was calculated considering the probability of Compton scattering in the front detector followed by photoelectric absorption in the back detector, and the differential cross-section for a given angle calculated with the Klein-Nishina formula.

3) Hybrid Imaging
Both events of coded aperture imaging and Compton imaging were used. The ML-EM reconstruction of the hybrid imaging, described in the work of Lee and Wehe [24], was used to combine the data from the two aforementioned imaging methods.

In the present study, the number of iterations for ML-EM was set to 20, which was selected empirically by investigating the variation of imaging resolution for the three imaging methods as a function of iteration number.

4. Mask thickness determination

In the case of the coded aperture system, the mask thickness is normally determined so as to serve enough opaqueness at the gamma-ray energy desired for its application. On the other hand, in the hybrid imaging system, a very thick mask is disadvantageous to Compton imaging, lowering its imaging sensitivity. Hence, the thickness of the mask should be determined based on a balance of system performances. Two metrics were chosen to determine the optimal thickness of the mask: minimum detectable activity (MDA) and imaging resolution. MDA and imaging resolution were surveyed for cases with different mask thicknesses (2, 4, 6, 8, 10 mm) and gamma-ray energies (100, 200, 400, 600, 800, 1000, 1200, 1600, 2000 keV) in order to investigate the relation between mask thickness and system performance.

4.1. MDA

MDA was considered as an indicator of imaging sensitivity to determine the optimal mask thickness for detection of low-level radioactivity. Note that the MDA is an index that can be compared between different imaging methods, whereas detection efficiency is inappropriate for comparison. This is because the detection efficiency is a measure of occurrence probability of effective event whose criterion is different according to the imaging method; the higher detection efficiency does not guarantee the higher imaging sensitivity. This can be also interpreted that the amount of information contained per effective event varies depends on the imaging method.

In the present study, receiver operation characteristic analysis was used to calculate the MDA of the imaging methods of the hybrid system, as motivated by the research of Tornga [25]. This method is applicable to all of the imaging methods of the hybrid system, considering that it is empirical and does not proceed according to the characteristics of any specific imaging method [26]. In this method, the MDA was determined as an activity that makes a false alarm rate (P_f) and a detection rate (P_d) meet a given margin. The P_f and P_d were calculated as the ratio that passes the signal-to-noise ratio (SNR) threshold among multiple images of background radiation and the source, respectively. The threshold was set to make the P_f meet the margin, and P_d was calculated for several source activity conditions.

MDA was calculated for a 1-min measurement of a point source at 3 m from the imaging system. The gamma yield of the source was assumed to be 1. The background radiation and gamma-ray source were simulated using Geant4, and 250 images were acquired for each activity condition within the range of 0–20 μCi. Then, the MDA was deduced according to the margins of $P_f = 0.1$ and $P_d = 0.9$.

The MDAs of the three imaging methods of the LAHGIS with different mask thicknesses are shown in Fig. 2. The MDA of Compton imaging was considered only for the energies of 400 keV or higher, since it was barely possible to acquire the Compton image at low energies (100 and 200 keV). The MDA of coded aperture imaging increased with the increase of the energy. The thicker mask showed the lower MDA for the coded aperture imaging throughout the energy, as expected. The MDA of the Compton imaging was mainly dependent on the energy, whereas it showed little dependence on the mask thickness.

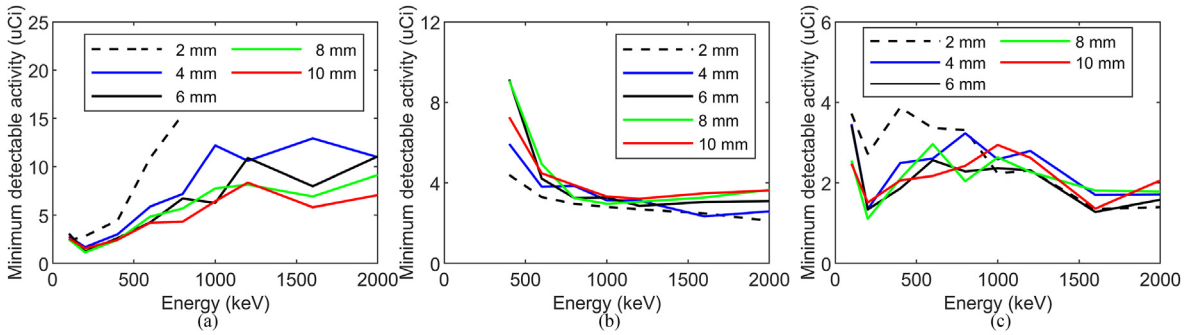

Fig. 2. MDAs of three imaging methods for different gamma-ray energies and mask thicknesses: (a) coded aperture imaging, (b) Compton imaging, (c) hybrid imaging.

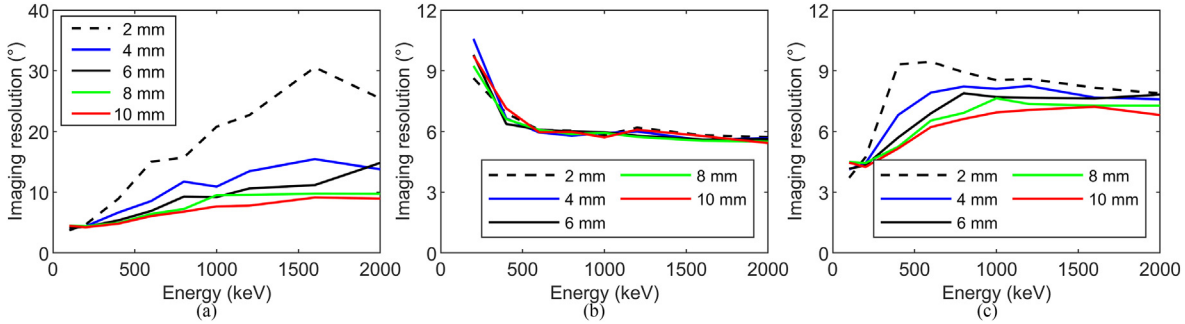

Fig. 3. Imaging resolution of three imaging methods for different gamma-ray energies and mask thicknesses: (a) coded aperture imaging, (b) Compton imaging, (c) hybrid imaging.

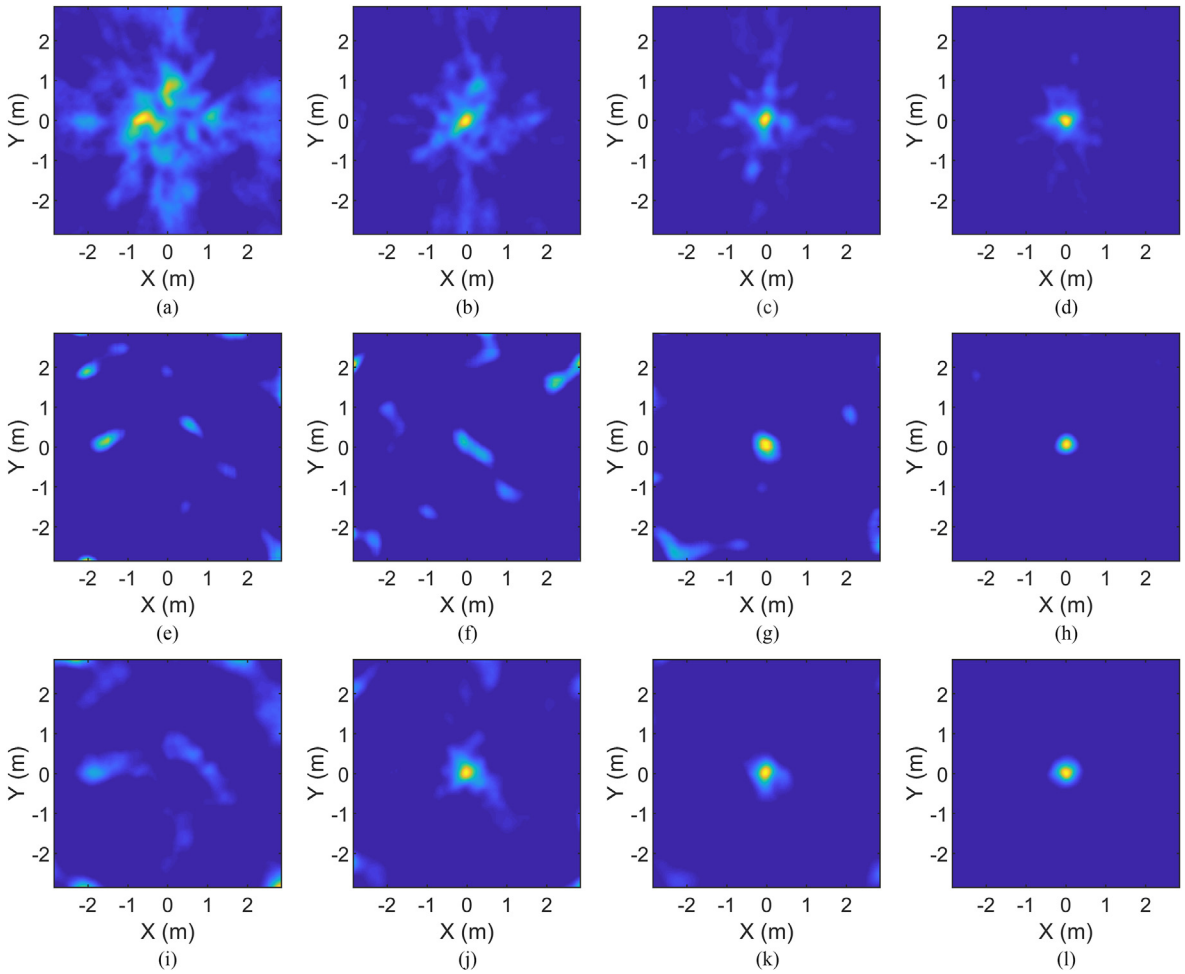

Fig. 4. ML-EM image of ^{137}Cs point source with different activities. Coded aperture imaging (a)–(d), Compton imaging (e)–(h), and hybrid imaging (i)–(l). Images for 0 μCi (a, e, i), 4 μCi (b, f, j), 10 μCi (c, g, k), and 20 μCi (d, h, l).

Hybrid imaging showed the lowest MDA among the three imaging methods for the entire energy range considered in the present study. The effect of mask thickness was found at low energies (100–400 keV); the 2-mm mask showed relatively higher MDAs than the other thickness conditions, providing insufficient attenuation at the energies where the coded aperture imaging has dominant effect on hybrid imaging. For the masks thicker than 2 mm, there was no significant correlation between MDA and mask thickness.

4.2. Imaging resolution

The imaging resolution was evaluated as the full-width half-maximum (FWHM, degrees) of the reconstructed image. In the simulation to acquire the images, again, a 1-min measurement of a point source at 3 m from the imaging system was assumed. The activity of the source was assumed to be 100 μCi.

The imaging resolutions evaluated for the three imaging methods are plotted in Fig. 3. For coded aperture imaging, the imaging resolution was greatly dependent on both the energy and the mask thickness. The imaging resolution at 100 keV was 4.2°, which was similar to the geometrically expected resolution (3.8°). The resolution of coded aperture imaging deteriorated with the increase of energy, and such effect was prominent for the thinner masks. For Compton imaging, the resolution was almost unaffected by the mask thickness. Finally, for hybrid imaging, the impact of mask thickness was found at intermediate energies (400–800 keV), where the resolution was significantly lower (i.e., higher in FWHM) for the 2 and 4 mm masks, whereas the masks with other thicknesses showed similar resolutions (around 6.4°).

4.3. Mask thickness determination

Mask thickness finally was determined from the results of the hybrid imaging. The MDA and imaging resolution of the hybrid imaging improved with the increase of mask thickness, then became constant when the mask thickness was greater than 4 and 6 mm, respectively. On the other hand, a thicker mask not only increases system weight and manufacturing cost but also increases artifacts in images for off-axis source locations such as uneven sensitivity by blocking photons that should pass through the open position of mask with the edge of neighboring mask element. Hence, in the present study, the mask thickness was determined to be 6 mm.

5. Imaging performance prediction

The localization performance of the designed system was assessed using Monte Carlo simulation for various conditions with different activities, energies, and positions. For each condition, the

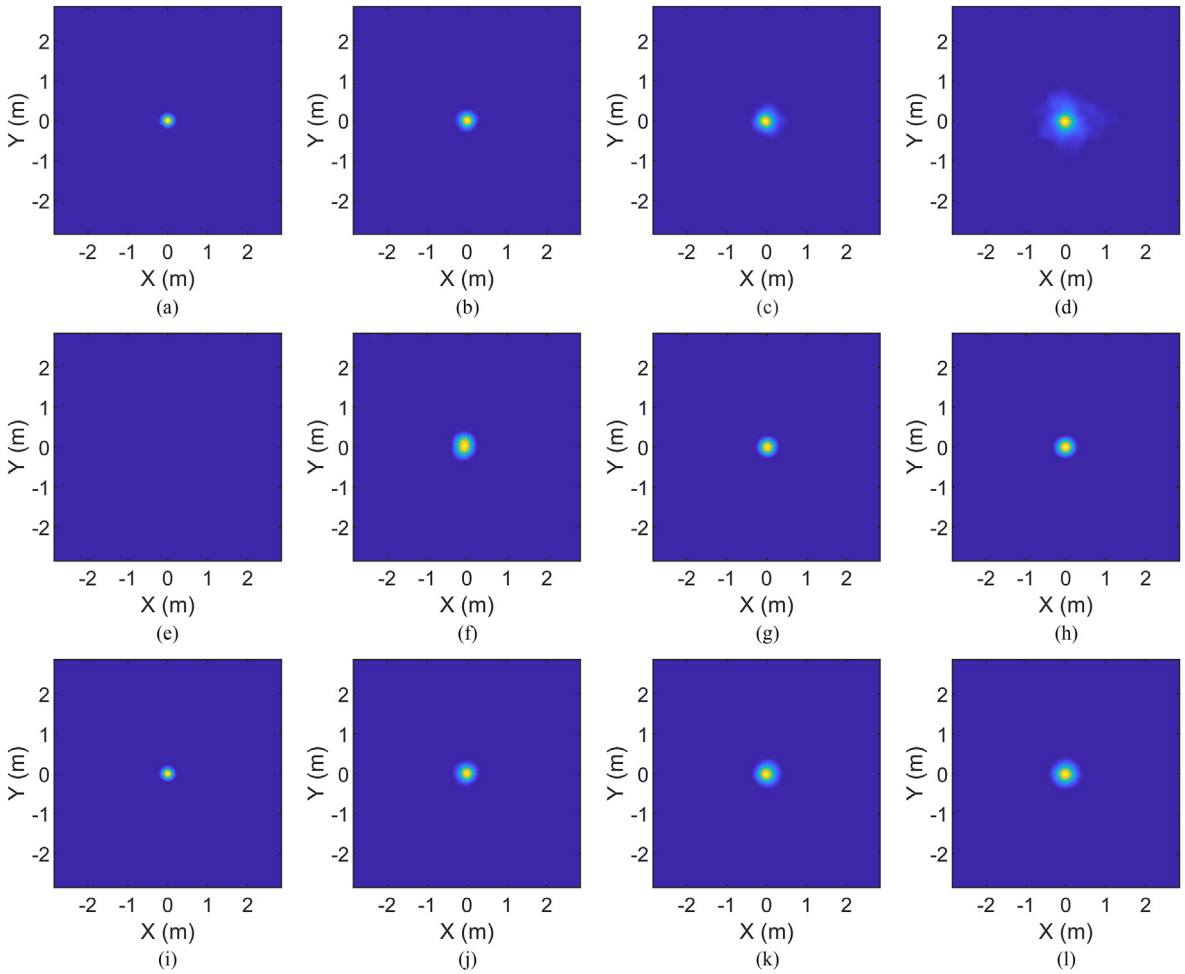

Fig. 5. ML-EM image of point source with different isotopes: ^{241}Am (a, e, i), ^{133}Ba (b, f, j), ^{137}Cs (c, g, k), and ^{60}Co (d, h, l), using coded aperture imaging (a–d), Compton imaging (e–h), and hybrid imaging (i–l).

images were acquired for 1-min measurement of the source at 3 m distance from the LAHGIS.

5.1. On-axis point source of varying activity

Fig. 4 shows the images of a ^{137}Cs point source of different activities (0, 4, 10, and 20 μCi) reconstructed using coded aperture imaging, Compton imaging, and hybrid imaging. Each of the reconstructed images was normalized to its maximum intensity: yellow for 1 and blue for 0; the same hereinafter. The coded aperture image for 0 μCi (i.e., imaging only background radiations, Fig. 4(a)) showed fluctuation, which makes it difficult to distinguish the signal of a source with low activity, as shown in Fig. 4(b). Compton imaging showed a high source-to-background-event ratio, meaning that it effectively distinguished the source gamma-rays from the background radiations. However, the limited counting statistics resulted in high-frequency noise, as shown in Fig. 4(f). The source was distinguished at 10 μCi, as shown in Fig. 4(g).

Hybrid imaging showed less blurring and high-frequency noise. The source was distinguishable even for 4 μCi (Fig. 4(j)), which capability is a clear advantage for detection of low-level radioactivity.

5.2. On-axis point source of varying energy

Fig. 5 shows images of the sources with different energies: ^{241}Am (59.5 keV), ^{133}Ba (356 keV), ^{137}Cs (662 keV), and ^{60}Co (1170 keV and 1330 keV). For the ^{133}Ba source emitting multiple energies of gamma rays, only the energy with the highest emission yield (i.e., 356 keV) was considered for image reconstruction. For the ^{60}Co source, both 1170 keV and 1330 keV gamma rays were considered. The activity of the source was assumed to be 100 μCi.

For coded aperture imaging, the four sources were all localized, but the background noise and blurring increased with the increase of the energy. The degradation of image quality originated from the mask attenuation decrease at higher energies: 100, 93, 68, and 46% attenuation at 59.5, 356, 662, and 1330 keV, respectively.

For Compton imaging, the ^{241}Am source was not imaged. Note that the ^{241}Am source was difficult to image using the designed system, due to the low penetration power of the low-energy photons in the front detector; the mean free path of 59.5 keV gamma-rays from ^{241}Am is only 0.04 cm in NaI(Tl). The ^{241}Am source is also difficult to image even using a Compton camera based on cadmium zinc telluride (CZT), considering that the high-Z material CZT shows a significant Doppler energy broadening effect in Compton scattering for low-energy photons, and that it has only a 1.7% probability of Compton scattering for 59.5 keV photons. The only feasible approach at present for imaging of ^{241}Am by Compton imaging seems to be to use position-sensitive silicon or germanium semiconductor detectors. Fig. 5(f) shows that the ^{133}Ba source was imaged using Compton imaging, but the image showed blurring

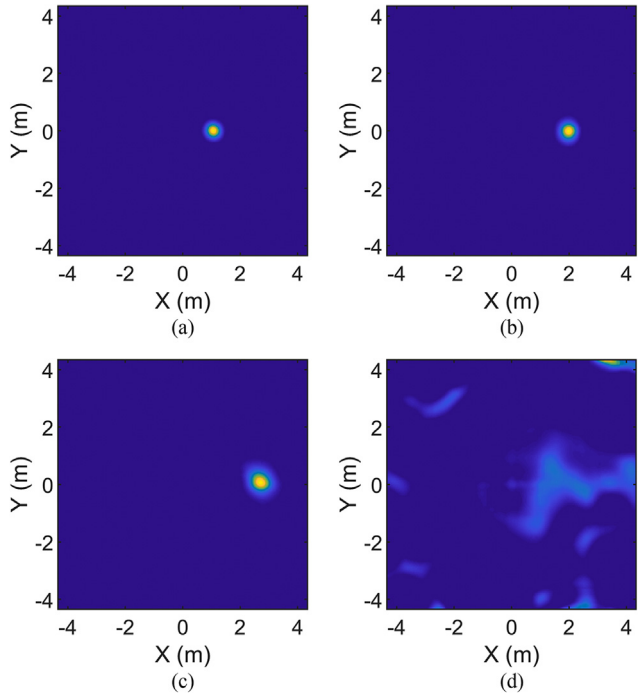

Fig. 6. Hybrid images of ^{137}Cs point source at different positions. The source was placed at a 3 m distance with an angle from axis of 20° (a), 40° (b), 60° (c), and 80° (d).

when compared with the Compton images of ^{137}Cs (Fig. 5(g)) and ^{60}Co (Fig. 5(h)).

With hybrid imaging, the images of all 4 sources were clearly acquired. Although some blurring was incurred compared with the Compton image, hybrid imaging showed moderately high imaging resolutions of 4.4, 5.9, 6.9, and 7.7° for ^{241}Am (59.5 keV), ^{133}Ba (356 keV), ^{137}Cs (662 keV), and ^{60}Co (1170 keV and 1330 keV), respectively.

Two studies [24,27] suggested the use of different imaging methods for different energies in consideration of image quality and computational cost. It seems, however, very advantageous to use hybrid imaging at all energies, given that it provides consistent performance over a wide energy range, and that it is less vulnerable to high-frequency noises observed on Compton images. The issue of computational cost, moreover, also has become less critical, due especially to the recent computational-power improvements.

5.3. Point source at different position

Fig. 6 shows hybrid images of the ^{137}Cs point source at 3 m distance with different angles from axis of 20°, 40°, 60°, and 80°, respectively. Although the blurring increased as the angle from the axis increased, it was able to locate the sources at 20°, 40°, and 60°, which are within the FOV, which was expected to be approximately ±65° based on the configurations of the mask and the detectors. However, the source at 80°, which is out of the FOV, did not appear on the image.

6. Conclusion

In the present study, a LAHGIS was designed to provide very high imaging sensitivity with moderately high imaging resolution over a broad energy range. Monte Carlo radiation transport simulations were conducted to understand how system geometry affects system performance. The performance of the LAHGIS was estimated for simulated sources at different activities, energies, and positions. Our results showed that hybrid imaging allows us to image low-activity sources that cannot be imaged by either coded aperture imaging or Compton imaging alone. The imaging resolution of the LAHGIS was estimated to be around 6° on the broad energy range of 59.5–1330 keV, using the ML-EM algorithm. Future work will include improving the calculation speed of the system responses for EM reconstruction, investigating 3-D imaging capability for near-field imaging, and combining the radiation image with contextual information such as visual images and range-mapping data.

Declaration of competing interest

The authors declare that they have no known competing financial interests or personal relationships that could have appeared to influence the work reported in this paper.

Acknowledgement

This work was supported by the National Research Foundation of Korea (NRF) grant funded by the Korean government (MSIT) (No. NRF-2017M2A8A4015258, NRF-2019M2D2A1A02059814) and Korea Institute of Energy Technology Evaluation and Planning (KETEP) grant funded by the Korean government (MOTIE) (No. 20191510301040).

References

[1] L.E. Smith, Z. He, D.K. Wehe, G.F. Knoll, S.J. Wilderman, Design and modeling of the hybrid portable gamma camera system, IEEE Trans. Nucl. Sci. 45 (1998) 963–969, 3.
[2] Y. Kim, J.H. Kim, J. Lee, C.H. Kim, Large-area Compton camera for high-speed and 3-D imaging, IEEE Trans. Nucl. Sci. 65 (11) (2018) 2817–2822.
[3] M. Galloway, A. Zoglauer, M. Amman, S.E. Boggs, P.N. Luke, Simulation and detector response for the high efficiency multimode imager, Nucl. Instrum. Methods A. 652 (1) (2011) 641–645.
[4] A. Kishimoto, J. Kataoka, T. Nishiyama, T. Fujita, K. Takeuchi, H. Okochi, H. Ogata, H. Kuroshima, S. Ohsuka, S. Nakamura, M. Hirayanagi, S. Adachi, T. Uchiyama, H. Suzuki, Performance and field tests of a handheld Compton camera using 3-D position-sensitive scintillators coupled to multi-pixel photon counter arrays, J. Instrum. 9 (2014).
[5] S. Takeda, A. Harayama, Y. Ichinohe, H. Odaka, S. Watanabe, T. Takahashi, H. Tajima, K. Genba, D. Matsuura, H. Ikebuchi, Y. Kuroda, T. Tomonaka, A portable Si/CdTe Compton camera and its applications to the visualization of radioactive substances, Nucl. Instrum. Methods A. 787 (2015) 207–211.
[6] C.G. Wahl, W.R. Kaye, W. Wang, F. Zhang, J.M. Jaworski, A. King, Y.A. Boucher, Z. He, The Polaris-H imaging spectrometer, Nucl. Instrum. Methods A. 784 (2015) 377–381.
[7] F. Hueso-González, G. Pausch, J. Petzoldt, K.E. Römer, W. Enghardt, Prompt gamma rays detected with a BGO block Compton camera reveal range deviations of therapeutic proton beams, IEEE Trans. Radiat. Plasma Med. Sci. 1 (1) (2017) 76–86.
[8] Y.S. Kim, J.H. Kim, H.S. Lee, H.R. Lee, J.H. Park, J.H. Park, H. Seo, C. Lee, S.H. Park, C.H. Kim, Development of Compton imaging system for nuclear material monitoring at pyroprocessing test-bed facility, J. Nucl. Sci. Technol. 53 (12) (2016) 2040–2048.
[9] Y. Shikaze, Y. Nishizawa, Y. Sanada, T. Torii, J. Jiang, K. Shimazoe, H. Takahashi, M. Yoshino, S. Ito, T. Endo, K. Tsutsumi, S. Kato, H. Sato, Y. Usuki, S. Kurosawa, K. Kamada, A. Yoshikawa, Field test around Fukushima Daiichi nuclear power plant site using improved Ce:Gd3(Al,Ga)5O12 scintillator Compton camera mounted on an unmanned helicopter, J. Nucl. Sci. Technol. 53 (12) (2016) 1907–1918.
[10] J.E. Gormley, W.L. Rogers, N.H. Clinthorne, D.K. Wehe, G.F. Knoll, Experimental comparison of mechanical and electronic gamma-ray collimation, Nucl. Instrum. Methods A. 397 (2) (1997) 440–447.
[11] L.E. Smith, C. Chen, D.K. Wehe, Z. He, Hybrid collimation for industrial gamma-ray imaging: combining spatially coded and Compton aperture data, Nucl. Instrum. Methods A. 462 (3) (2001) 576–587.
[12] M. Galloway, A. Zoglauer, S.E. Boggs, M. Amman, A combined Compton and coded-aperture telescope for medium-energy gamma-ray astrophysics, Astron. Astrophys. 614 (2018) A93.
[13] S.R. Gottesman, E.E. Fenimore, New family of binary arrays for coded aperture imaging, Appl. Optic. 28 (20) (1989) 4344–4352.
[14] R. Accorsi, F. Gasparini, R.C. Lanza, A coded aperture for high-resolution nuclear medicine planar imaging with a conventional Anger camera:

experimental results, IEEE Trans. Nucl. Sci. 48 (6) (2001) 2411–2417.
[15] S.J. Kaye, W.R. Kaye, Z. He, 4π coded aperture imaging using 3d position-sensitive CdZnTe detectors, in: 2008 IEEE Nuclear Science Symposium Conference Record, 2008, pp. 711–713.
[16] Y.S. Kim, J.H. Kim, H.S. Lee, C.H. Kim, Position-sensitive NaI(Tl) detector module for large-area Compton camera, J. Kor. Phys. Soc. 72 (1) (2018) 26–32.
[17] E. Caroli, J.B. Stephen, G. Di Cocco, L. Natalucci, A. Spizzichino, Coded aperture imaging in X- and gamma-ray astronomy, Space Sci. Rev. 45 (3) (1987) 349–403.
[18] R. Accorsi, Design of a Near-Field Coded Aperture Cameras for High-Resolution Medical and Industrial Gamma-Ray Imaging (Ph.D. dissertation), Massachusetts Inst. Tech., 2001.
[19] U.B. Jayanthi, J. Braga, Physical implementation of an antimask in URA based coded mask systems, Nucl. Instrum. Methods A. 310 (3) (1991) 685–689.
[20] J. Allison, K. Amako, J. Apostolakis, P. Arce, M. Asai, T. Aso, E. Bagli, A. Bagulya, S. Banerjee, G. Barrand, B.R. Beck, A.G. Bogdanov, D. Brandt, J.M.C. Brown, H. Burkhardt, P. Canal, D. Cano-Ott, S. Chauvie, K. Cho, G.A.P. Cirrone, G. Cooperman, M.A. Cortés-Giraldo, G. Cosmo, G. Cuttone, G. Depaola, L. Desorgher, X. Dong, A. Dotti, V.D. Elvira, G. Folger, Z. Francis, A. Galoyan, L. Garnier, M. Gayer, K.L. Genser, V.M. Grichine, S. Guatelli, P. Guèye, P. Gumplinger, A.S. Howard, I. Hřivnáčová, S. Hwang, S. Incerti, A. Ivanchenko, V.N. Ivanchenko, F.W. Jones, S.Y. Jun, P. Kaitaniemi, N. Karakatsanis, M. Karamitros, M. Kelsey, A. Kimura, T. Koi, H. Kurashige, A. Lechner, S.B. Lee, F. Longo, M. Maire, D. Mancusi, A. Mantero, E. Mendoza, B. Morgan, K. Murakami, T. Nikitina, L. Pandola, P. Paprocki, J. Perl, I. Petrović, M.G. Pia, W. Pokorski, J.M. Quesada, M. Raine, M.A. Reis, A. Ribon, A. RistićFira, F. Romano, G. Russo, G. Santin, T. Sasaki, D. Sawkey, J.I. Shin, I.I. Strakovsky, A. Taborda, S. Tanaka, B. Tomé, T. Toshito, H.N. Tran, P.R. Truscott, L. Urban, V. Uzhinsky, J.M. Verbeke, M. Verderi, B.L. Wendt, H. Wenzel, D.H. Wright, D.M. Wright, T. Yamashita, J. Yarba, H. Yoshida, Recent developments in Geant4, Nucl. Instrum. Methods A. 835 (2016) 186–225.
[21] J.H. Kim, J. Lee, Y. Kim, H.S. Lee, C.H. Kim, Development of hybrid shielding system for large-area Compton camera: a Monte Carlo study, Nucl. Eng. Technol. 52 (10) (October 2020) 2361–2369.
[22] L.A. Shepp, Y. Vardi, Maximum likelihood reconstruction for emission tomography, IEEE Trans. Med. Imag. 1 (2) (1982) 113–122.
[23] E. Munoz, J. Barrio, J. Bernabeu, A. Etxebeste, C. Lacasta, G. Llosa, A. Ros, J. Roser, J.F. Oliver, Study and comparison of different sensitivity models for a two-plane Compton camera, Phys. Med. Biol. 63 (13) (2018) 135004.
[24] W. Lee, D. Wehe, Hybrid gamma ray imaging—model and results, Nucl. Instrum. Methods A. 579 (1) (2007) 200–204.
[25] S.R. Tornga, Mobile, Hybrid Compton/coded Aperture Imaging for Detection, Identification and Localization of Gamma-Ray Sources at Stand-Off Distances, Univ. of New Mexico, 2013.
[26] A. Poitrasson-Rivière, B.A. Maestas, M.C. Hamel, S.D. Clarke, M. Flaska, S.A. Pozzi, G. Pausch, C.-M. Herbach, A. Gueorguiev, M.F. Ohmes, J. Stein, Monte Carlo investigation of a high-efficiency, two-plane Compton camera for long-range localization of radioactive materials, Prog. Nucl. Energy 81 (2015) 127–133.
[27] L.J. Meng, D.K. Wehe, Feasibility study of using hybrid collimation for nuclear environmental imaging, IEEE Trans. Nucl. Sci. 50 (2003) 1103–1110.